Journal of Nanobiotechnology

RESEARCH Open Access

Zinc-doped curcumin carbon dots promote infected wound healing with photodynamic via the VEGF signaling pathway

Yifan Zhao[1,2†], Jia Liu[1,2†], Lingxiang Sun[1,2†], Haiyan Liu[1,2], Xi Chen[1,2], Xuedong Deng[1,2], Yilin Ping[1,2], Wenze Han[1,2], Jing Wang[1,2], Feng Tian[1,2], Jingyu Yan[1,2], Xiuping Wu[1,2*] and Bing Li[1,2*]

Abstract

Management of bacterial infected wounds remains challenging due to the open, susceptibility to infection and delayed healing characteristics of damaged wounds, and there is an urgent need for non-antibiotic-based wound healing strategies. Here, we describe zinc-doped curcumin carbon dots (CCDs) as a novel nanoscale photosensitizer, which was applied in photodynamic therapy (PDT) to promote infected wound healing by modulating various cellular functions. The PDT generation of reactive oxygen species (ROS) effectively inactivates the source of infection without drug resistance, effectively inhibiting the propagation of bacteria and the spread of inflammation in the wound. In addition, CCDs have the ability to promote cell proliferation and extension, accelerate blood vessel formation and collagen deposition, and significantly improve wound healing efficiency by modulating the VEGF signaling pathway. These features create a favorable environment for skin regeneration and synergistically accelerate infected wound healing. We believe it has great potential to address antibiotic misuse and effectively manage infected wounds.

Keywords Carbon dots, Wound healing, Antimicrobial therapy, Photodynamic therapy, Curcumin, VEGF signaling pathway

Introduction

Skin wounds due to various causes go through four phases: hemostasis, inflammation (including antimicrobial activity and inflammatory factor secretion), proliferation and tissue remodeling/epithelial reformulation [1]. Skin wounds are susceptible to bacterial infection when exposed to the external environment, resulting in delayed wound healing [2]. Antibiotics are now widely used to treat infected wounds. However, misuse of antibiotics can lead to the development of drug resistant strains, which not only reduces the effectiveness of treatment, but can even lead to the emergence of super bacteria [3]. Therefore, new strategies that are free of drug resistance are essential for bacterial wound treatment.

Photodynamic therapy (PDT) has been used to treat cancer, infectious diseases, and skin and oral conditions, including acne vulgaris, rosacea, and genital warts [4, 5]. PDT uses a combination of photosensitizers and specific wavelength lasers that result in the generation of reactive oxygen species (ROS) that affect cell signaling and selectively cause damage or death in target tissues and

†Yifan Zhao, Jia Liu and Lingxiang Sun are equally to the work as co-authors.

*Correspondence:
Xiuping Wu
77wxp@163.com
Bing Li
libing1975vip@163.com

Full list of author information is available at the end of the article

Graphical Abstract

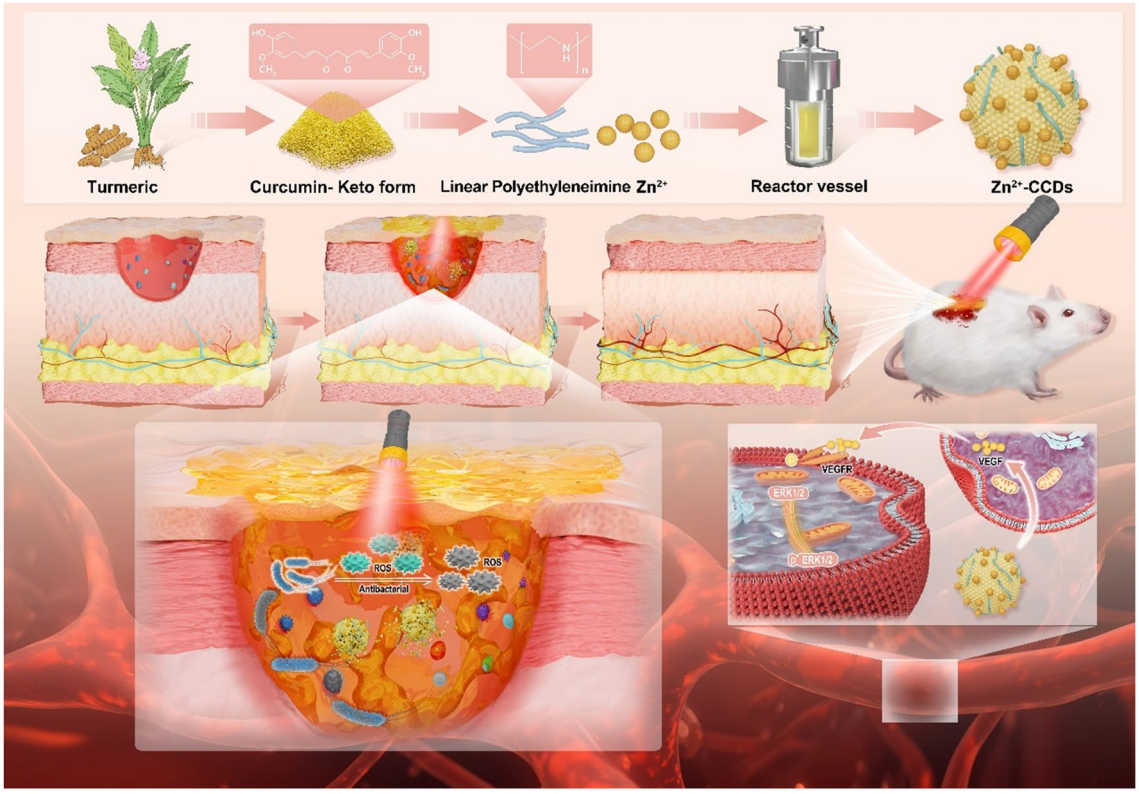

microorganisms without treatment resistance. The main product of PDT is ROS, which can mediate the regulation of intracellular signaling in vivo [6]. The selection of appropriate photosensitizers as well as wavelength-matched light sources is crucial in the application of PDT for disease treatment.

Carbon dots (CDs) as a novel photosensitizer with low toxicity, fast metabolism and high efficiency in ROS generation [7, 8]. Recent studies have shown that CDs have emerged as a promising biomedical material with excellent optical properties as well as good biocompatibility, and have great potential for antimicrobial therapy and wound healing promotion. The ultra-small size endows CDs with more exposed active sites and functional groups for modification [9]. As the field has evolved, CDs derived from herbs have been used in disease treatment due to their inspiration from traditional Chinese medicine [10, 11]. The broad spectral absorption of CDs in the UV to NIR region gives them the ability to achieve photodynamic anti-microbial effects under visible/natural light activation [12]. Meanwhile, it has been shown that the raw materials used in the synthesis of CDs retain a portion of their efficacy structure during the carbonization process, thereby transferring properties to the final product. Curcumin (CUR) is a class of biologically active natural compounds isolated from the turmeric plant. Turmeric is rich in bioactive curcuminoids - including curcumin (77%), dimethoxy-curcumin (17%) and dimethoxy-curcumin (3–6%). Among them, curcumin (1,7-bis-(4-hydroxy-3-methoxyphenyl)-hepta-1,6-diene-3,5-dione) is the most important constituent, and as a lipophilic polyphenol is used as an anticancer, antimicrobial, anti-inflammatory, anti-aging and other [13]. CUR is also currently used in PDT as an effective photosensitizer against a wide range of bacteria. However, the therapeutic potential of CUR is limited by its low solubility in aqueous media, poor bioavailability and pharmacokinetic profile [14]. In order to solve these problems, the synthesis of nanoscale CDs as photosensitizers from CUR may be a very feasible route. What's more, compared with other CDs prepared from pure chemical compounds and complex surface functionalization, CUR is more suitable for large-scale production as a precursor with abundant sources, simple preparation routes, and green environment, which is expected to be used as a novel photosensitizer for counteracting the problem of delayed healing of bacterial infected wounds.

As one of the essential metallic elements for humans and bacteria, zinc has many important physiological roles [15, 16]. In the case of bacteria, excess zinc interacts with

the sulfhydryl groups of bacterial respiratory enzymes to inactivate them, and ultimately electron transfer mismatches in the respiratory chain led to the production of intracellular ROS in the bacterial cell. This accumulation of ROS induces irreversible damage to bacterial DNA as well as lipid peroxidation of bacterial membranes, leading to bacterial death [17]. For human body, zinc-based nanomaterials are easily degraded and metabolized, meanwhile, appropriate amount of zinc can activate various signaling pathways and induce cells to secrete stromal chemokines, transforming growth factors, vascular endothelial growth factors, and platelet growth factors, which play an important biological function in the maintenance of venous vascular network and hematopoietic development [18, 19]. Zinc has been shown to act as a nutrient or proliferation stimulating signal for damaged tissues, and Wu et al. used zinc sulfonate and black phosphorus to accelerate wound healing and bone regeneration under photothermal conditions. The presence of zinc increased the sensitivity of bacteria to photothermal heat and promoted wound healing through the sustained slow release of Zn^{2+} [20].

In this study, we report a kind of carbon nanocomposites prepared by using CUR as a raw material in combination with zinc acetate (Zn-CCDs, referred to as CCDs). Applied as an effective photosensitizer for photodynamic killing of Gram-positive and Gram-negative bacteria while promoting vascular regeneration and healing of infected wounds, the high biocompatibility and stability of CCDs enable the long-lasting effect of the whole composite system at the wound. Meanwhile, CDs as photosensitizers retain the antibacterial, anti-inflammatory and photosensitizing activities of CUR, improving the overall bioavailability. Zinc-loaded CCDs can achieve the purpose of promoting angiogenesis and reducing vascular pathological disorders through slow release of zinc ions. Meanwhile, Zn^{2+} doping changed the internal electronic environment of CDs, and the increased surface defects could promote the effective separation of photogenerated electrons and holes, thus enhancing the photodynamic therapeutic effect of CCDs [21, 22]. What's more, CCDs can accelerate wound healing by activating the VEGF pathway and promoting tissue regeneration. Therefore, we believe that this is a novel strategy to effectively promote the recovery of infected wounds.

Materials and methods

Materials

Curcumin, zinc acetate and polyethyleneimine were obtained from Macklin Reagent, CCK-8 kit, cell live/dead staining reagent, cytoskeletal staining reagent, and matrix gel were purchased from Thermo Fisher Scientific. The water used in the experiments was deionized water, and the reagents were used directly without any purification. Escherichia coli (*E. coli*, ATCC 25922) and Staphylococcus aureus (*S. aureus*, ATCC 25923) were purchased from Beijing Three Drugs Science and Technology Development Company (China). The human umbilical vein endothelial cells (HUVEC) and L929 cells were purchased from the Clinical Research Center of Shanxi Medical University. Male Sprague Dawley (SD) rats (8 weeks old) were purchased from Beijing Vital River Laboratory Animal Technology Co.

Preparation of CCDs

In the present study, one-step hydrothermal method was used to obtain zinc ion doped carbon dots of curcumin origin. 2 ml of polyethyleneimine, 1 g of curcumin, 0.5 g of zinc acetate were dissolved in 45 ml of deionized water and transferred to a reactor. The reaction was carried out in a vacuum drying oven at 200 °C for 10 h to obtain a brownish yellow liquid. The brownish yellow solution obtained was centrifuged at 12,000 rpm for 10 min to remove large particles. The remaining solution was filtered through a 0.22 μm and dialyzed in deionized water for 48 h. The molecular retention capacity of the dialysis bag was 1000 Da. The final liquid was freeze-dried to obtain a brown Zn-CCDs powder and used for further analysis.

Characterization of CCDs

The UV-Vis absorption spectra of CCDs were characterized using a TU-1901 117 spectrophotometer. In addition, a JEM-2100 transmission electron microscope was used to characterize the morphology and structural features of CCDs. The composition and surface functional groups of CCDs were analyzed by Fourier transform infrared instrument (FT-IR). Transmission electron microscopy (TEM) was used to detect CCDs after dialysis and to characterize their appearance and structure. The crystal structure of CCDs was determined by X-ray diffraction (XRD). In addition, XPS analysis was performed using X-ray photoelectron spectroscopy in order to identify the elemental composition of the CCDs.

Antibacterial performance test

S. aureus and *E. coli* suspensions ($1 \times 10\text{^}6 \sim 1 \times 10\text{^}7$ CFU/mL) were treated in groups. The control group was left untreated, the Laser group was subjected to laser irradiation (660 nm, 5 min), the CCDs group and the Laser + CCDs group were co-cultured with CCDs and only the Laser + CCDs group was subjected to laser irradiation (660 nm, 5 min). Diluted bacterial suspensions (100 μL, 1:1000 dilution) of each culture were inoculated onto agar plates. Bacterial colonies formed were counted and recorded after 12 h of incubation.

Sterile filter paper sheets of 7 mm diameter were soaked with PBS buffer or different concentrations (1, 10,

20, 50, 100, 200 μg/mL) of CCDs solution. The suspensions of *S. aureus* and *E. coli* (1 × 10^7 CFU/mL) were dipped in cotton swabs and then spread evenly on TSB agar plates. The diameters of the inhibition rings were photographed and recorded after incubation at a constant temperature of 37 ℃ for 12 h.

Scanning electron microscope (SEM) was used to observe the morphological changes of bacteria after treatment in different groups. The suspensions of *S. aureus* and *E. coli* were treated with CCDs for 4 h and laser irradiation for 10 min, and the bacteria of different treatment groups were collected by centrifugation and washed twice with PBS. Glutaraldehyde solution was added to the bacterial precipitates to fix the bacterial surface morphology. The immobilized bacteria were washed with PBS buffer and then dehydrated with 30%, 50%, 70%, 80%, 90% and 100% ethanol for 15 min, and then resuspended in anhydrous ethanol and placed on the silicon wafer. Finally, the samples were sprayed with gold to obtain SEM images of the bacteria, and then the obtained images were processed with pseudo-color using Photoshop CS6.

The CCDs were co-cultured with bacterial suspensions of *S. aureus* and *E. coli* (2 mL, 1.5 × 10^8 CFU/mL) for 4 h and subjected to different treatments. Bacteria from different treatment groups were collected and stained with SYTO 9 (green fluorescence) and PI (red fluorescence) in the dark and incubated away from light for 30 min. The final bacterial precipitates were washed twice with PBS and resuspended. The resuspended bacterial droplets were added to glass slides, observed under a confocal laser scanning microscope (CLSM) and photographed for documentation.

ROS production in two bacteria was imaged using the classical ROS fluorescent probe 2',7'-Dichlorodihydrofluorescein diacetate (DCFH-DA). Bacterial suspensions were incubated for 4 h under different treatment conditions, centrifuged and washed three times before adding a final concentration of 20 μL DCFH-DA and incubated for 30 min at 37 °C. Subsequently centrifuged and washed three times, then resuspended in PBS and fixed on slides with glycerol gelatin sealing solution for CLSM observation.

S. aureus and *E. coli* (1 × 10^6) in logarithmic growth phase were inoculated on sterile crawls in 24-well plates. After different group treatments, the plates were incubated for 48 h. After the bacterial biofilm was formed, the plates were carefully washed with PBS for three times, to which the crystal violet dye was added. After 10 min, the plates were washed twice with PBS, dried naturally and photographed and recorded with a digital camera. Afterwards, crystal violet dye was dissolved using glacial acetic acid and the absorbance of the solution was tested at 570 nm.

S.aureus and *E. coli* suspensions (1 × 10^6 CFU/mL) were treated in groups. The control group was left untreated, Laser group was irradiated with laser, CCDs and Laser + CCDs groups were co-cultured with CCDs and only Laser + CCDs group was irradiated with laser and antibiotic group was treated with standard antibiotic Ciprofloxacin. After different treatments, bacteria were collected by centrifugation at 5000 rpm for 5 min and rinsed thoroughly with PBS. After resuspending the bacteria with PBS, PI apoptosis kit were added to them and incubated at 37 ℃ in a dark environment for 15 min. The bacteria were washed three times with PBS and then resuspended in 0.2 mL of PBS to be used for flow-through assay in the experimental group. The prepared samples were detected by flow cytometry and the data were analyzed by Flow Jo software.

Cytotoxicity assay

To detect the cytotoxicity of CCDs on HUVEC and L929, cell viability was assayed using the CCK-8 assay. Briefly, HUVEC cells (5 × 10^4) were homogeneously inoculated in 96-well plates overnight. After continued incubation for 1, 3, and 5 days for different concentration (10, 20, 50, 100, 200, and 500 μg/mL) groups treated accordingly, the medium was discarded and rinsed thoroughly with PBS. Subsequently, basal medium containing CCK-8 reagent was added to each well so that the final concentration of CCK-8 in each well was 10%. The 96-well plate was taken out after several hours, and the absorbance value of each well was measured at 450 nm with an enzyme labeler, and the OD value of the experimental group was compared with that of the control group to calculate the cell proliferation rate with the formula: cell proliferation rate = (OD value of the experimental group / OD value of the control group) × 100%. Another set of CCK-8 assays were set up with Control group, Laser group, CCDs group (set to the optimal concentration of CCDs) and Laser + CCDs group. The remaining treatments were as above.

Live/dead assay

HUVEC cells (1 × 10^5) were uniformly inoculated in 24-well plates overnight. The different treatment groups (Control, Laser, CCDs and Laser + CCDs) were treated accordingly and continued to incubate for 24 h. Subsequently, the well plates were rinsed thoroughly with PBS and the configured live/dead staining solution was added for 15 min. After washing the excess dye with PBS, the cells were observed with CLSM.

Scratch assay

A linear scratch model was used to assess the migration ability of HUVEC and L929 cells. HUVEC cells were inoculated in 12-well plates at a cell density of 5 × 10^4/well overnight, and linear scratches were scraped with

a sterile p200 pipette. CCDs were added to the medium and incubated for 4 h. The cells were then irradiated with laser for 10 min and incubated continuously for 0 h, 12 h, 24 h and 48 h. Finally, the cells were gently washed with PBS and observed under a light microscope. L929 cells were treated as above, and the time intervals between incubation and observation were 0 h, 24 h and 36 h. The area of the scratches was measured using ImageJ software and the scratches' healing rate was calculated. Scratch healing rate (%) =(A0-A1/A0) ×100%, where A1 and A0 are the scratch areas at different times of culture and 0 h, respectively.

Transwell migration assay

HUVEC and L929 cells were inoculated into the upper chamber of the transwell at a density of 1 × 10^5 cells/well overnight, the medium in the lower chamber of the two groups was replaced with complete medium containing CCDs and the other groups were treated accordingly. 24 h later, the transwell chambers were fixed with 4% paraformaldehyde for 15 min, and then the chambers were immersed with 1% crystal violet solution and washed three times. The non-migrated cells in the upper chamber were wiped away with a cotton swab. The migration was observed and recorded under a light microscope.

Tube formation assay

To evaluate the angiogenic ability of HUVEC in vitro, we performed tube formation assay. The method was as follows: first, the 96-well plate was pre-cooled in a -20 ℃ refrigerator, and Matrigel (Corning, USA) was kept in a 4 ℃ refrigerator for spare time. The pre-cooled 96-well plate was placed in an ice box, and then 50 μL of Matrigel was added to each well to confirm the absence of air bubbles. The matrix was solidified at 37 ℃ for 30 min. Then, the HUVEC cells were cultured through different treatment groups for 6 h. The cells were observed and photographed under a light microscope, and three regions were randomly selected, and the number of junctions and the total tube length were calculated using ImageJ software.

Immunofluorescence assay

HUVEC and L929 cells were mixed with CCDs at a cell density of 4 × 10^5/mL and transferred to cell culture dishes for co-culture for 48 h. Cells were fixed with 4% paraformaldehyde for 30 min at room temperature, washed twice with PBS, permeabilized with Triton X-100 for 15 min, and then added to immunostaining blocking solution and incubated for 60 min. Next, cells were incubated with VEGF (ab52917, 1:500), overnight at 4 ℃, then incubated with fluorescent secondary antibody under dark conditions for 1 h at room temperature, washed with PBS, and stained with DAPI for 5 min. Finally, cells were imaged under CLSM.

EdU cell proliferation assay

1 × 10^5 HUVEC cells were inoculated in each well of a 12-well plate. After different treatment groups were treated and incubated for 12 h, the cells were treated with 10 μM EdU reagent (KeyGEN BioTECH, China) for 2 h at 37 °C. After rinsing with PBS, cells were fixed with 4% paraformaldehyde solution for 15 min. After permeabilization with Triton X-100 for 15 min, the cells were incubated with reaction reagent for 30 min at room temperature. The nuclei were labeled with DAPI reagent. Finally, the cells were observed under CLSM.

Quantitative real-time RT-PCR (qRT-PCR) analysis of cells

Total RNA was extracted using an RNA extraction kit (Vazyme, China). cDNA was reverse transcribed from the extracted RNA using a PrimeScript RT kit (Vazyme, China). RT-qPCR experiments were performed using a quant studio 6 Flex real-time PCR system (Thermo Fisher Scientific) and a SYBR@Premix Ex Taq (sparkjade, China). VEGF and TGF-β genes were detected using β-actin as endogenous control gene, the primer sequence is shown in Table S1.

Transcriptome sequencing and data analysis

To further elucidate the mechanism by which CCDs promote skin wound healing, we performed transcriptome analysis. Cells were incubated with or without CCDs solution added to HUVEC. RNA was extracted by treating the cells with Trizol reagent and stored at -80 °C for sequencing. RNA-seq was performed with Illumina HiSeq X10 (Illumina, USA) and normalized using the fragment count per kilobase per million reads method. Gene ontology and KEGG pathway enrichment analyses were performed via the free online bioinformatics platform (www.bioinformatics.com.cn).

The cells seeded in the culture dish were divided into three groups: Control group (without any treatment), Laser + CCDs group (after uptake of CCDs, laser irradiation for 10 min), and Inhibitor group (co cultured with VEGFR2 inhibitor SU1498 for 2 h, then added to the culture medium containing CCDs, and laser irradiation after uptake). The scratch assay, transwell assay, and VEGF immunofluorescence staining steps are the same as above. The steps of immunoblotting are as follows: collect the proteins from three groups of HUVEC cells with different treatments using cell lysate, and conduct protein gel experiments on SDS-PAGE gel. All antibody models and sources used are listed in Table S2.

In vivo study

All the animal experiments were performed in accordance with the Guidelines for the Care and Use of Laboratory Animals of Shanxi Medical University and approved by the Animal Ethics Committee of Shanxi Medical University. In vivo antimicrobial and wound healing promotion experiments were performed on a rat bacterial infection wound model. SD rats (250 ± 10 g) were randomly divided into 4 groups ($n = 4$): Control group, Laser group (660 nm, 10 min,), CCDs group, and Laser + CCDs group (660 nm, 10 min). On day 0, the rats were anesthetized intraperitoneally with 0.6% sodium isopentylbarbitone (0.12 mL/10 g), and a perforator (2 cm in diameter) was used to create a full trauma on the back of the rats, and 60 μL of *S. aureus* suspension (2 × 10^7 CFU/mL) was added dropwise to the wound. The groups were treated on day 1, 3, 6, 9, and 13, and photographs of the rats were taken on day 0, 2, 5, 10, and 14. The rats were anesthetized on day 14, and traumatic skin tissues were collected. The wound healing rate was calculated as: healing rate = (day 0 wound area - day n wound area/day 0 wound area) × 100%. The skin tissues on day 1 and day 10 were placed in sterile saline with full vortex shock to release bacteria, and the bacteria-containing solution was sampled on agar plates (37 ℃, 24 h). After euthanasia, important organs of rats were removed, and the skin tissues were subjected to H&E staining, Masson staining, Sirius Red Staining and immunofluorescence and histochemical staining (CD31, CD206, and iNOS).

Statistical analysis

All data were statistically analyzed and the results were expressed as mean ± standard deviation (SD). Statistical differences were determined by one-way ANOVA and student-t test. In all cases, a significant difference was indicated if $p < 0.05$.

Results and discussion

Preparation and characterization of CCDs

Using curcumin powder as the main raw material, combined with zinc ions provided by zinc acetate and nitrogen rich polyethyleneimine, a brownish yellow carbon dots powder was finally obtained through a classic one-step hydrothermal method (Fig. 1A). During the synthesis process, some properties of the raw materials were well transferred to the new products. At the same time, various elements and electron pairs undergo reaction pairing and binding, giving CCDs new and unique properties.

Fig. 1B and C are TEM images of composite nanoparticles, showing that CCDs were spherical and had a uniform particle size distribution, with an average of 2.65 ± 0.3 nm. It can be seen that CCDs had detailed lattice fringes, and the lattice spacing corresponds to the (001) crystal plane of graphite at 0.21 nm, which was similar to the results reported in the literature [23]. The XRD pattern of the composite nanoparticles in Fig. 1D showed a clear peak of CCDs at 22.77 °, corresponding to the (002) crystal plane of graphite carbon, indicating that CCDs had a complete crystal structure and have been successfully prepared [24]. The surface of CCDs had a positive potential of 28.9 (Fig. S1), and the presence of multiple functional groups on the surface facilitates the response of CCDs to laser irradiation in various wavelength bands. Studies have shown that CCDs with positive potential can firmly bind to bacterial surfaces with negative potential, improving their bactericidal performance [25].

The FT-IR spectrum shown in Fig. 1E exhibited peaks at 3409, 3255, 2931, 1604, and 1457 cm^{-1}, corresponding to the stretching vibrations of - OH/- NH, C-H, C = C, and N-H groups, respectively. The peak at 879 cm^{-1} could be considered a characteristic peak of ZnO, which is related to specific vibration modes in the ZnO crystal structure. Therefore, the significant water solubility of CCDs can be attributed to the presence of abundant hydrophilic groups on their surfaces, which also confirmed the existence of Zn [26]. The chemical composition and functional groups of CCDs were analyzed using X-ray photoelectron spectroscopy (XPS). The XPS full spectrum in Fig. 1F showed that CCDs are mainly composed of C, N, O, and Zn elements. The high-resolution XPS spectrum of C1s can be decomposed into three peaks with binding energies of 288.1 eV, 255.5 eV, and 284.5 eV, respectively. These peaks represented C = O/C-N, C-O/C-N, and C-C/C = C, respectively (Fig. 1G). The N1s band deconvolution peaks at 399.9 eV and 399.0 eV correspond to graphite nitrogen and pyrrole nitrogen, respectively (Fig. 1H) [27]. The peaks of O1s at 532.3 eV and 530.9 eV correspond to C = O and O-H (Fig. 1I) [26]. Fig. 1J showed the high-resolution XPS spectrum of Zn2p, with two peaks at binding energies of 1044.4 eV and 1021.4 eV. These peaks corresponded to the spin orbit dipoles of Zn 2p3/2 and Zn 2p1/2, respectively, indicating that zinc doped CCDs contain zinc in the two positive valence state [28]. The abundant nitrogen in CCDs comes from polyethyleneimine, which can provide the necessary elements for the synthesis of carbon dots. Meanwhile, nitrogen atom doping, as an efficient and convenient method, provides abundant active sites and functional groups on the surface of CCDs, which broadens the application scope of carbon dot nanomaterials. Because the doping of nitrogen plays an important role in improving the fluorescence properties and photosensitizing activity of carbon dots, it may lead to a 20 nm redshift of the maximum fluorescence emission position of the carbon dots and an increase in the emission intensity of the carbon dots, a property that is of great significance

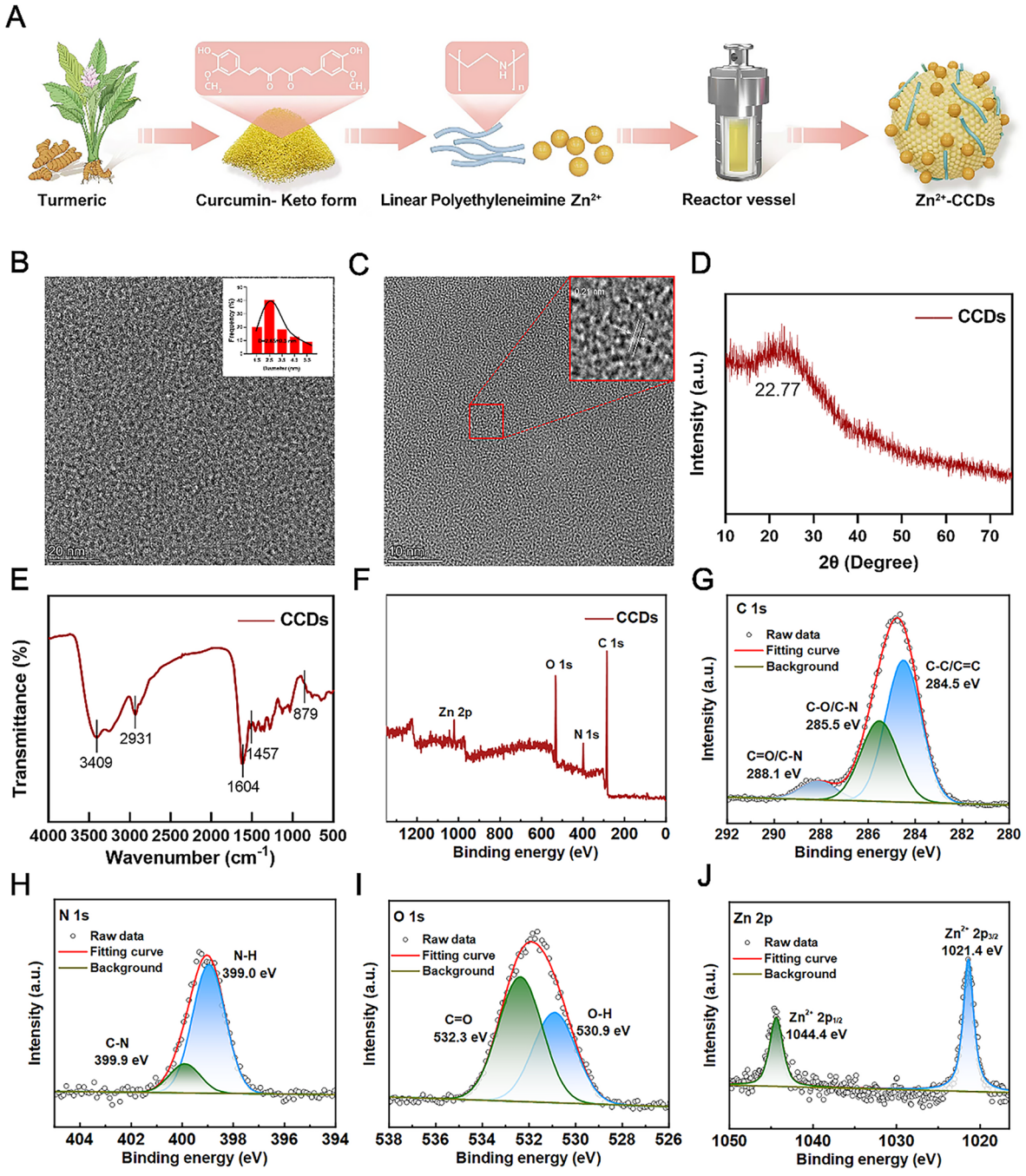

Fig. 1 Characterization of CCDs. (**A**) Schematic illustration of the preparation process of CCDs; (**B**, **C**) TEM images and nanoparticle size analysis; (**D**) XRD pattern of CCDs; (**E**)FT-IR spectra of CCDs; (**F**) XPS full-scan spectrim of CCDs; XPS high-resolution scans of C1s (**G**), N1s (**H**), O1s (**I**) and Zn 2p (**J**) of CCDs.

for the use of carbon dots as photosensitizers [29]. All these results demonstrated the successful synthesis of Zn-CCDs nanoparticles.

Antibacterial property

Due to the damaged barrier, exposing the wound to the complex daily environment increases the risk of bacterial infection. *S. aureus* is ubiquitous on the surface of the skin and in the living environment and is one of the most common infectious agents of the skin [30, 31]. In addition, many studies have shown that *E. coli* is increasing the incidence of wound infections [32, 33]. Therefore, *S. aureus* and *E. coli* were selected as representative strains of Gram-positive and Gram-negative bacteria for the study of the antimicrobial properties of CCDs in PDT of infected wounds. The CCDs composites with an overall positively charged nature were firmly attached to the negatively charged bacterial surfaces by

electrostatic interaction. At the same time, a part of the bacteria ingested the nanoscale CCDs into the intracellular space, and PDT effect was produced under laser irradiation to achieve the killing effect. As shown in Fig. 2C, different concentrations of CCDs formed inhibitory rings with varying diameters, indicating that the inhibitory effect of CCDs on bacteria was stronger as the concentration increased (1–200 μg/ml). Digital photographs of *S. aureus* and *E. coli* forming colonies on agar plates in different treatment groups are shown in Fig. 2A. The number of colonies in the Laser + CCDs group was significantly less than that of the control group, with a reduction of 3–4 orders of magnitude. It can be seen that laser irradiation or CCDs alone had some inhibitory effect on the growth of both bacteria, but the effect was poor.

CCDs, as a novel photosensitizer, are capable of producing ROS under laser irradiation for photodynamic effects. In order to investigate the specific mechanism of bacterial killing by Laser + CCDs, we used DCFH-DA as a reactive oxygen probe to probe the ROS production in bacteria after different treatments. The presence of ROS in bacteria oxidizes the non-fluorescent DCFH-DA to the strong green fluorescent substance DCF [34]. Fig. 2E showed a weak green fluorescence in *E. coli* and *S. aureus* after ingestion of CCDs, and a bright green fluorescence in almost all bacteria after PDT, representing the production of a large amount of ROS after photodynamic therapy. Fig. 2G showed the SEM images of the two bacteria after PDT, with pseudo-colors being used to highlight the regions of interest. It can be seen that the surface of the bacteria in the Control group was smooth and full, with clear and intact boundaries, able to form a complete biofilm structure. In the Laser + CCDs group, it was obvious to see that the bacterial cell membranes were wrinkled, collapsed, with blurred boundaries, and in some cases the contents were in the form of a jet, which is a typical manifestation of the severe damage to the bacteria caused by the high concentration of ROS. The surface of *S. aureus* was twisted and compressed and deformed, but basically remained intact and spherical. In contrast, the degree of destruction of *E. coli* was more significant, the cell membrane was strongly contracted and ruptured, and the shell lost its intact morphology. This difference may be due to the fact that the phosphomimic acid cell wall of the outer layer of Gram-positive bacteria restricted the expansion and rupture of the bacterial body to a certain extent. A part of the large amount of ROS generated by photodynamic force acted directly on the cell membrane structure, while the other part attacked the organelles and nucleic acids, causing irreversible damage and thus killing the bacteria. This is the classic type I mechanism in PDT, which played an important role in the whole treatment system [35]. This therapeutic mechanism significantly slowed the development of bacterial drug resistance and prevents the formation of bacterial biofilms. We hypothesize that Zn^{2+} was released from the composite nanoparticles and disrupted the cell membrane by neutralizing the negative charge of the cell membrane [36]. At the same time, the composition of CUR can also inhibit the adhesion of bacteria to a certain extent, greatly reducing the risk of bacterial infection [37].

In Fig. 2G, live/dead fluorescence staining was performed on the bacteria in different treatment groups to visually distinguish the survival status of bacteria by red and green fluorescence. Compared with the Control group and the Laser group, the rest of the treatment groups had obvious red fluorescence, indicating that the inactivated bacteria accounted for a great proportion. In contrast, there was almost no green fluorescence in the Laser + CCDs treatment group, and this killing showed the same trend in the quantitative analysis of Fig. 2F. Some studies have already reported that PDT has different selectivity for Gram-negative and Gram-positive bacteria due to differences in the surface structure of bacterial cell membranes. In general, photosensitizers are more likely to penetrate the porous cell walls of Gram-positive bacteria to produce ROS to act as bactericidal agents [38, 39].

Exploration of the mechanism of CCDs-mediated PDT also revealed that the ROS produced by this treatment modality inhibits the formation of bacterial biofilm, which improves the permeability of CCDs and enhances the killing effect on deep-seated bacteria [40]. At the same time, this treatment reduces the risk of developing drug resistance by not targeting the characteristic stages of the bacterial metabolic phase and impeding the formation of biofilm——the barrier. The results of biofilm formation inhibition experiments showed (Fig. S2) that the density and structure of the two bacterial biofilms were significantly disrupted after Laser + CCDs treatment and antibiotic Ciprofloxacin treatment, showing almost the same trend, indicating that the effect of CCDs-mediated PDT is almost comparable to that of the standard antibiotics in terms of antimicrobial activity. Therefore, CCDs as photosensitizers can effectively induce ROS burst to inhibit biofilm formation and significantly kill bacteria.

Fig. S3 showed the results of flow cytometry analysis of CCDs mediated PDT on *E. coli* and *S. aureus*. It can be seen that almost all (99.1%, 99.5%) of the bacteria in the control group did not undergo apoptosis, which means that most of the bacteria in the group were in a viable state. Both the Laser group (3.34%, 8.17%) and the CCDs group (19.5%, 20.4%) showed varying numbers of stained cells with apoptotic signals, but apoptotic signals were stronger in the CCDs group, which means both of the treatments can both kill certain bacteria, but the killing ability of CCDs is stronger. After the

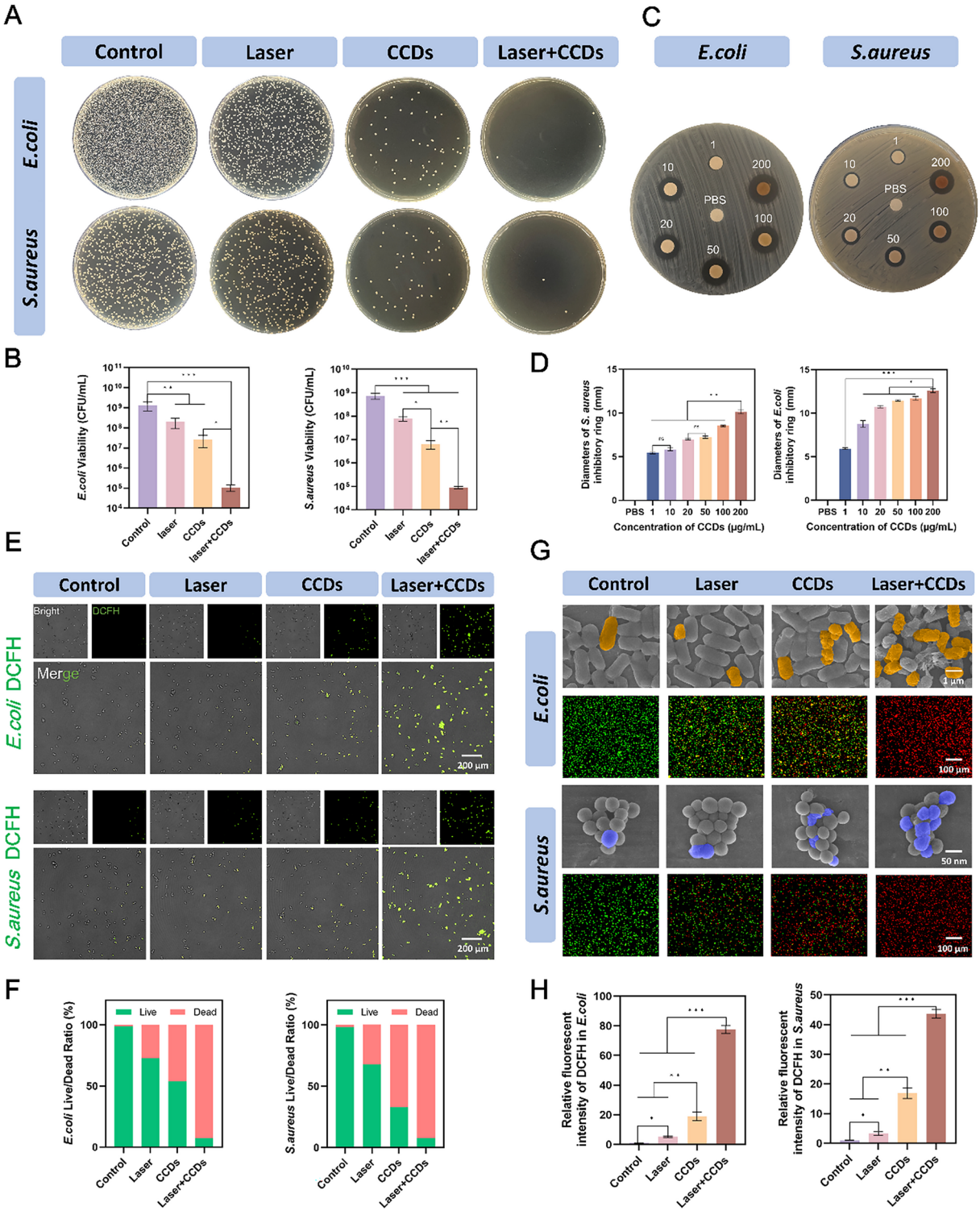

Fig. 2 Antimicrobial properties. (**A**) Plate count images of *E. coli* and *S. aureus* in each group; (**B**) Quantitative analysis of the number of *E. coli* and *S. aureus* colonies; (**C**) Ring of inhibition images of *E. coli* and *S. aureus* in each group. The different conditions are PBS buffer or CCDs solution with concentrations of 10, 20, 50, 100, 200 μg/mL; (**D**) Quantitative analysis of diameters of inhibition ring of *E. coli* and *S. aureus* with different concentration of CCDs; (**E**) ROS probe fluorescent staining images of *E. coli* and *S. aureus* in each group; (**F**) Quantitative ratios of live and dead *E. coli* and *S. aureus*; (**G**) SEM images and live/dead fluorescent staining images of *E. coli* and *S. aureus* in each group; (**H**) Quantitative analysis of the intensity of ROS fluorescence of *E. coli* and *S. aureus*. (*$p < 0.05$, **$p < 0.01$, ***$p < 0.001$)

addition of laser irradiation, the survival rate of both bacteria in the Laser + CCDs group decreased dramatically, showing similar results to the antibiotic Ciprofloxacin. Among them, the apoptotic cells of *E. coli* increased to 32.3% (37.8% in the Ciprofloxacin group) while those of *S. aureus* increased to 31.4% (36.9% in the Ciprofloxacin group). The results showed that CCDs-mediated PDT had excellent antibacterial effects, even similar to those of standard antibiotics, and was effective in inducing apoptosis and inhibiting further propagation of bacteria. CCDs adhered to the bacterial organisms and entered into the intracellular compartment, and then ROS generated by the PDT damaged the internal biomolecules of bacteria and eventually led to bacterial death, which is in line with the conclusions drawn from the previous studies [41].

Promote cell migration and vascularization

Damaged tissues begin to proliferate and repair after the inflammatory phase, and blood vessels are important channels for transporting nutrients and growth factors [42]. Classical scratch and transwell migration assays were chosen to examine the angiogenic potential of HUVEC and L929 cells after PDT, and a matrigel-based tube formation assay for HUVEC was designed to further investigate.

The cytotoxicity of CCDs was first explored by standard CCK-8 assay. Fig. S4 showed that CCDs at different concentrations did not exhibit significant toxicity after 1, 3 and 5 days of co-culture with HUVEC. Interestingly, CCDs at a concentration of 200 μg/ml were able to significantly promote the proliferation of endothelial cells to some extent. This concentration was chosen as the standard concentration for subsequent assays. Fig. 3C and Fig. S5 showed that the Laser + CCDs treatment group promoted the proliferation of HUVEC and L929 cells, respectively. The CCDs treatment group also slightly raised the viability of both cells. The remaining treatment groups showed no significant difference. Based on the results of live/dead cell staining of HUVEC cultured with CCDs for 24 h, almost no dead cells (red fluorescence) were observed in each treatment group, as shown in Fig. 3A. EdU staining of HUVEC showed similar results to those of CCK-8. EdU is a thymine deoxyribonucleoside analog that is capable of replacing the thymine deoxy nucleus doped into de novo and synthesized DNA during DNA synthesis. Therefore, the amount of newly synthesized DNA was examined by the EdU-related kit to reflect the proliferation status of the cells. The results showed (Fig. 3B) that the Laser + CCDs group exhibited bright red fluorescence, and the rest of the treatment groups had weaker fluorescence intensity (Fig. 3E), indicating that CCDs in the presence of laser irradiation could indeed promote HUVEC propagation and facilitate wound recovery.

Scratch healing by endothelial cells is central to the process of tissue re-formation during wound healing. As shown in Fig. 4A and Fig. S6A, both HUVEC and L929 cells in the Laser + CCDs group exhibited optimal healing after treatment. Notably, the CCDs group also showed some promotion in the scratch assay for both cells. The data in Fig. S5 and Fig. S6D quantified the healing rate of scratches, showing the same trend. After 24 h of incubation, the migration rates of HUVEC and L929 cells were significantly higher in the Laser + CCDs group than in the other treatment groups (Fig. 4B and S6B). Endothelial cells are components of blood vessels and play a crucial role in angiogenesis. The matrix gel tube formation assay performed to assess the angiogenic capacity showed (Fig. 4C) that Laser + CCDs-treated HUVEC showed a significant increase in tube length and number of junctions after 6 h compared with the Control group (Fig. 4E and S8), which may be attributed to the release of Zn^{2+} as well as the generation of controlled ROS. Overall, CCDs have the ability to promote cell migration under laser irradiation, which is beneficial for accelerating the wound healing process.

As a well-known angiogenesis related factor, vascular endothelial growth factor (VEGF) induces proliferation, migration, and angiogenesis of epidermal and endothelial cells. During angiogenesis, VEGF is essential for the recruitment, maintenance, proliferation, migration and differentiation of endothelial cells [43, 44]. Therefore, we expressed the expression of VEGF protein in cells of different treatment groups by fluorescence staining (Fig. 3D and S6C). The results showed that HUVEC and L929 cells exhibited bright red fluorescence in the cytoplasm after PDT, and CCDs-treated group also had strong red fluorescence, while the ones in the Control group showed almost no expression. The quantitative analysis of fluorescence intensity in Fig. 3F and Fig. S6F is consistent with the above. The relative gene expression levels of VEGF and TGF-β in the two types of cells (Fig. 4F and G and S9, S10) were closer in the CCDs and Laser + CCDs groups, and significantly higher than those in the Control and Laser groups. Zinc, as an essential trace element, plays an important biological function in the maintenance of the venous vascular network and the development of hematopoiesis [45]. Our study confirmed that CCDs stimulate angiogenesis by slowly releasing Zn^{2+}, which is consistent with previous reports [46]. And the aforementioned toxicity test also showed that Zn^{2+} in the composite nanoparticles also did not affect the normal cell viability. The above results indicated that CCDs exhibit complex and active regulation of angiogenesis after laser irradiation.

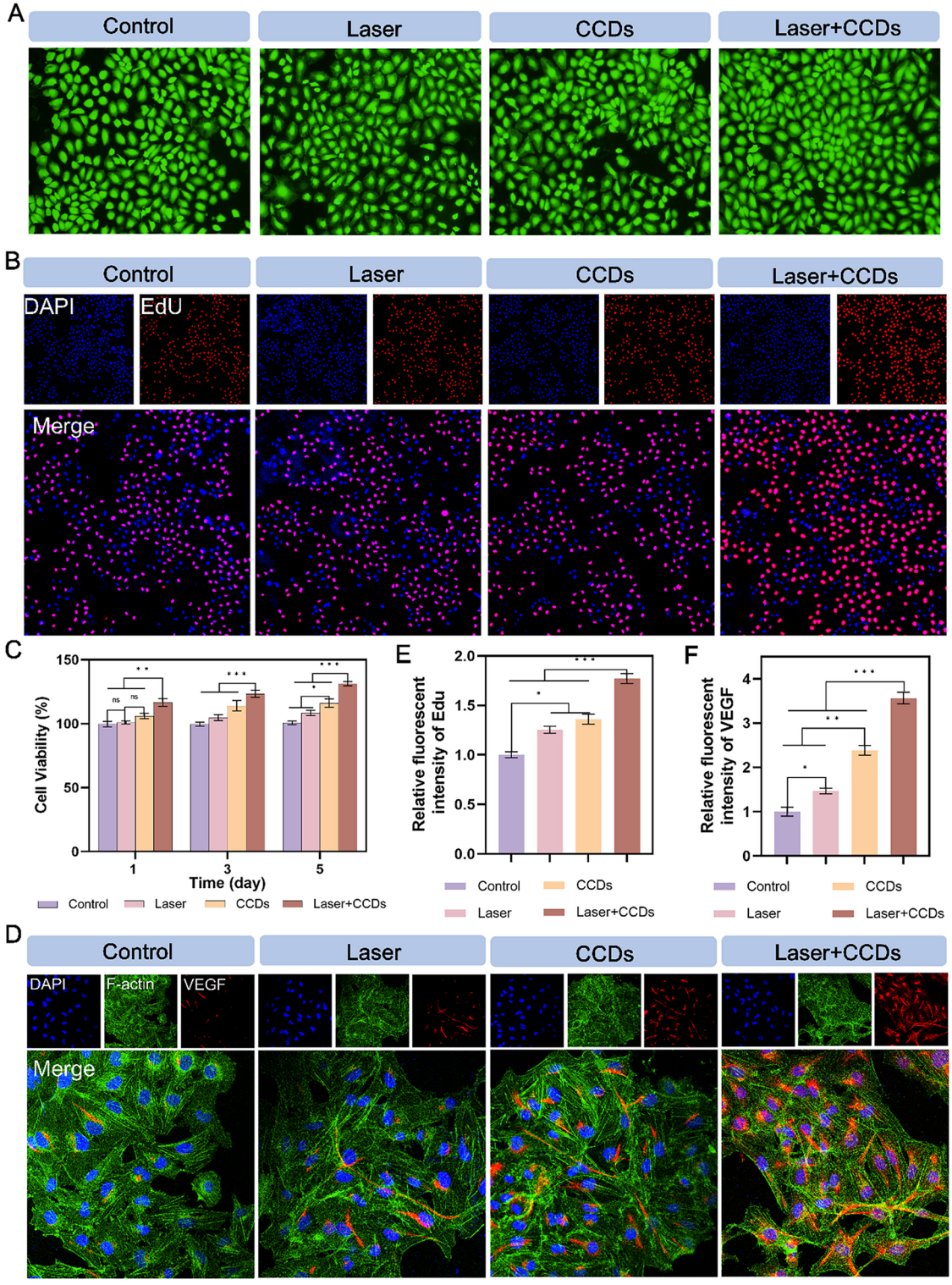

Fig. 3 Promotion of HUVEC proliferation and angiogenic protein expression. (**A**) Live/dead staining images of HUVEC; (**B**) Fluorescence images of HUVEC EdU staining in each group; (**C**) Cell proliferation in CCK8 assay at 1, 3 and 5 days; (**D**) Immunofluorescence staining images of VEGF protein in each group; (**E**) Quantitative analysis of fluorescence intensity of EdU staining in each group; (**F**) Quantitative analysis of immunofluorescence intensity of VEGF protein in each group. (*$p < 0.05$, **$p < 0.01$, ***$p < 0.001$)

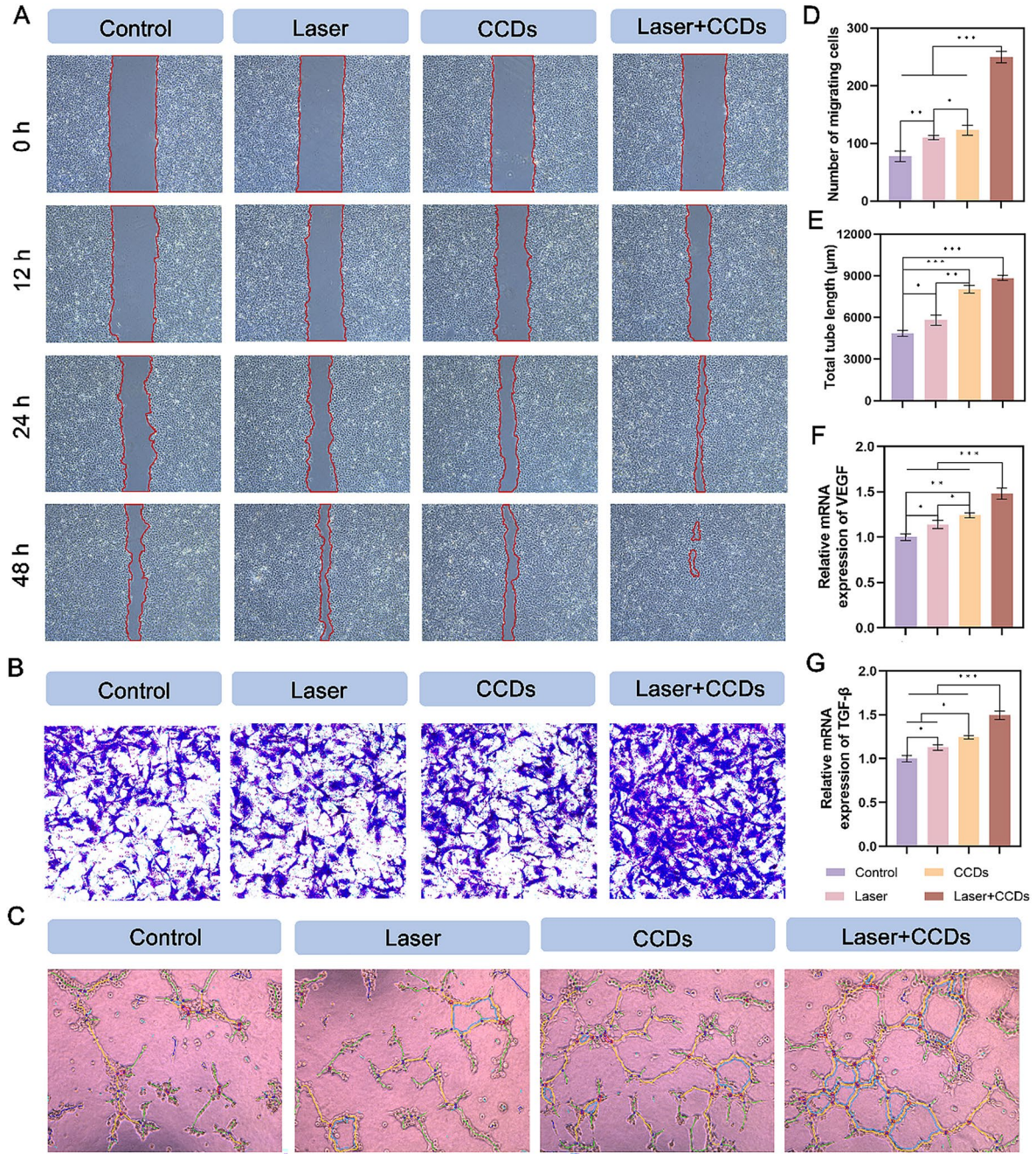

Fig. 4 Promotion of HUVEC migration and angiogenic property. (**A**) Representative images of HUVEC scratching assay, the red underlined portion represents the scratched area; (**B**) Representative images of HUVEC transwell migration assay in each group; (**C**) Images of HUVEC tube formation assay; (**D**) Quantitative analysis of the number of migrating cells in each group; (**E**) Quantitative analysis of the total tube length formation in each group; (**F**) Quantitative analysis of relative mRNA expression of VEGF; (**G**) Quantitative analysis of relative mRNA expression of TGF-β. (*$p < 0.05$, **$p < 0.01$, ***$p < 0.001$)

The potential mechanism of accelerated infected wound healing

Wound healing is a complex process involving interactions between different cell types, growth hormones, cytokines, antioxidants, and a steady supply of metal ions (e.g., calcium, zinc, and magnesium). After skin damage, a number of cellular systems and signaling pathways are activated in the wound to protect the body [47]. In order to elucidate the possible regulatory mechanisms of Zn^{2+}-doped curcumin carbon dots to promote infected wound healing, we performed transcriptome analysis on cells from two different treatment groups (Control and Laser + CCDs groups).

Principal Component Analysis (PCA) results showed that samples from each group were clustered independently, verifying that the two treatment groups did

produce differences (Fig. 5A). Volcano plots showing up- and down-regulated genes generated after different treatments in the Control and Laser + CCDs groups exhibited significant differential gene expression between the different groups (Fig. 5B). To further analyze these differential gene expressions, we performed Gene Ontology (GO) enrichment analysis. GO typically characterizes genes at three levels: cellular component (CC), biological process (BP), and molecular function (MF). Fig. 5C showed the top enriched items in each category, which mainly include down-regulated expression of immune response, inflammatory response aspects and up-regulated vascular morphology and proliferation of vascular smooth muscle, endothelial phylogeny and cell adhesion.

Meanwhile, Kyoto Encyclopedia of Genes and Genomes (KEGG) enrichment analysis was applied to analyze the potential signaling pathways. Fig. 5D showed in detail the pathways with high relevance and their names, and the up-regulated signaling pathways include VEGF signaling pathway, cell adhesion molecule signaling pathway and mitogen-activated protein kinase (MAPK) signaling pathway.

It is well known that the VEGF signaling pathway is closely related to collagen deposition and angiogenesis. And the MAPK signaling pathway promotes keratinocyte proliferation and migration, and plays an important role in transmitting extracellular stimulatory signals to cells and mediating cellular biological responses (e.g., cell growth, migration, proliferation, differentiation, and apoptosis). On the other hand, CCDs photodynamic therapy also down-regulated some of the pathways, including the IL-17 signaling pathway, and the tumor necrosis factor (TNF) signaling pathway, which are associated with the inflammatory response and regulation of tissue destruction. The heatmap in Fig. 5E showed the names of the genes with specific changes for major differences in the above pathways. Specific names and interconnections regarding the genes screened for greater differential expression by GO enrichment analysis are displayed in Fig. 5F. These results suggested that the VEGF signaling pathway may be activated during PDT with CCDs to promote cellular angiogenesis, thereby accelerating wound healing.

MAPK is very important in transmitting signals of extracellular stimuli to the cells and mediating cellular biological responses (e.g., cell growth, migration, proliferation, differentiation and apoptosis). Mammalian MAPKs can be categorized into four subfamilies: ERK1/2, p38, JNKs and ERK5 [48]. Multiple differential genes of the ERK pathway were enriched in the MAPK signaling pathway. VEGF is the most important angiogenic stimulator and plays important roles in angiogenesis and neointima formation, including causing cell proliferation, inhibiting apoptosis, increasing vascular permeability, and vasodilation. Genes upregulated in the VEGF/VEGFR2 pathway include VEGFA, PLCG2, and PLA2G4C. Among them, PLA2G4C is also involved in the ERK pathway.

To investigate whether the MAPK and VEGF signaling pathways were potential mechanisms and further validate the above hypothesis to promote infectious wound healing, we validated them in terms of genes and proteins as well as phenotypes. VEGFR2 inhibitor (SU19498) was used to test the reliability of the sequencing results. The scratch test results after 12 h in Fig. 6A showed that the scratch area of the Control group and the Inhibitor group has not changed much compared to 0 h, with only a trace amount of healing. The Laser + CDs group showed a significant promoting effect on healing. The migration assay in Fig. 6C also showed the same trend, with only the Laser + CCDs group showing a large number of cells migrating to the lower chamber. This proves that VEGFR2 inhibitor hindered the signaling process on this pathway, thereby inhibiting the growth and migration of HUVEC cells. The above effects were also demonstrated by VEGF immunofluorescence and immunoblotting (Fig. 6E and G), confirming the importance of VEGF in endothelial cell growth and various physiological activities. The VEGF/VEFGR2 pathway is closely related to the MEK1/2/ERK1/2 signaling pathway, and one of the downstream pathways of the VEGF signaling pathway is to mediate cell proliferation through the ERK pathway [49]. By WB detection of VEGF, VRGFR2, phosphorylated VRGFR2, phosphorylated ERK1/2, and ERK1/2, we found that the protein expression levels of the Control group and pathway inhibitor group were almost the same, whereas the expression of each index was significantly increased in the PDT group with CCDs. It is particularly noteworthy that the application of VEGFR2 inhibitor (SU19498) can effectively inhibit the phosphorylation of VEGFR2, resulting in a significant decrease in the expression levels of downstream VEGF proteins p-VEGFR2/VEGFR2 and p-ERK1/2/ERK1/2 in the Inhibitor group. In summary, the above results indicated that CCDs promote endothelial cell growth and wound healing through the VEGF/VEGFR2/ERK1/2 pathway.

The results suggested that CCDs photodynamic therapy exerts its role in promoting vascular endothelial cell growth by modulating VEGF/VEGFR2 and its downstream MEK1/2/ERK1/2 signaling axis. Thus, wound healing cannot be achieved without precise regulation including hemostasis, inflammation, proliferation and remodeling sequences.

Evaluation of in vivo infected wound healing

Based on the efficacy of CCDs with PDT in killing bacteria and promoting the proliferation and repair of

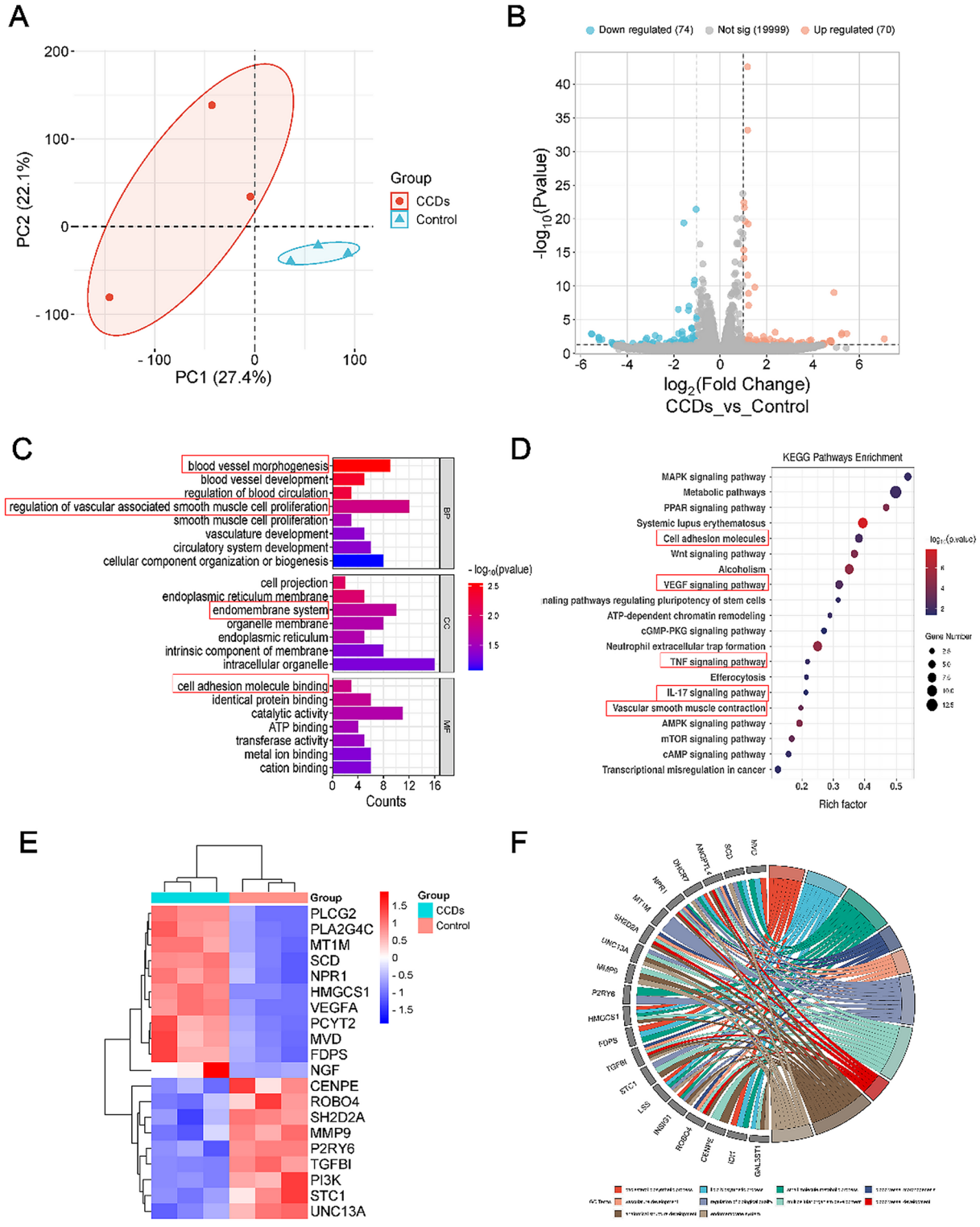

Fig. 5 Gene expression profiles and regulatory mechanisms in promoting infectious wound healing. (**A**) PCA analysis of samples; (**B**) Volcano plot with up- and down-regulated genes; (**C**) Representative top 22 differentially expressed terms analyzed by the Gene Ontology (GO) enrichment method; (**D**) Representative top 20 up- or down-regulated pathways analyzed by KEGG pathway method; (**E**) The Heatmap analysis and (**F**) circus of differentially expressed genes involved in multiple pathways

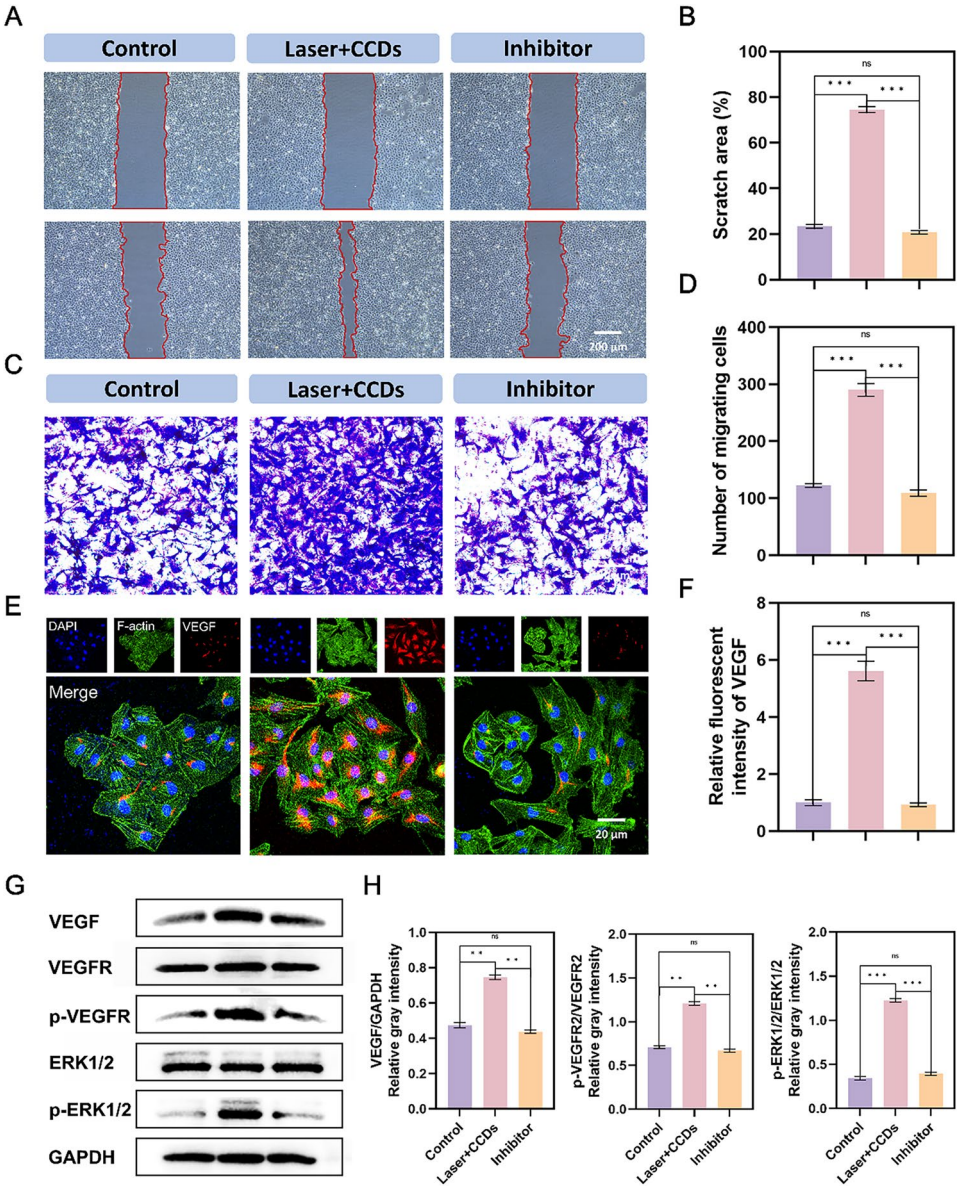

Fig. 6 Verification of VEGF signaling pathway mechanism in HUVEC. (**A**) Representative images of scratching assay, the red underlined portion represents the scratched area; (**B**) Quantitative analysis of scratch area closure in each group; (**C**) Representative images of migration assay in each group; (**D**) Quantitative analysis of the number of migrating cells in each group; (**E**) Immunofluorescence staining images of VEGF protein in each group; **(F)** Quantitative analysis of immunofluorescence intensity of VEGF protein in each group;**(G)** Expression of VEGF, VEGFR, ERK1/2, phospho-VEGFR, -ERK1/2 and GAPDH, as well as the gray intensity analysis in HUVEC; (**H**) Quantitative analysis of (**G**). (*$p < 0.05$, **$p < 0.01$, ***$p < 0.001$)

endothelial cells obtained in vitro, we further used infected wound rats to study their repair effect in vivo.

First, a whole-layer rat skin defect model with a diameter of 2 cm was created, and *S. aureus* bacterial suspension was applied to the wound surface to establish an infection model. Saline and CCDs were injected into the infected wounds for treatment (named Control group, Laser group, CCDs group, and Laser + CCDs group, respectively), and the parameters of the laser used in the treatment were 660 nm, 10 min, and 500 mW/cm^2. Digital photographs of the wound area at different time points and overlapping images of the simulated healing are shown clearly in Fig. 7A and B. After 24 h, the wound the wound became visibly infected. The results showed that at the end of the first treatment (day 2), the surface of the Control and Laser groups was ulcerated and oozing, bleeding was apparent, and no obvious scab formation was seen, while the CCDs and Laser + CCDs groups showed obvious signs of healing, with the bleeding stopping and the formation of thicker healing scabs. After 14 days, the wounds of the CCDs and Laser + CCDs groups were almost healed but accompanied by varying degrees

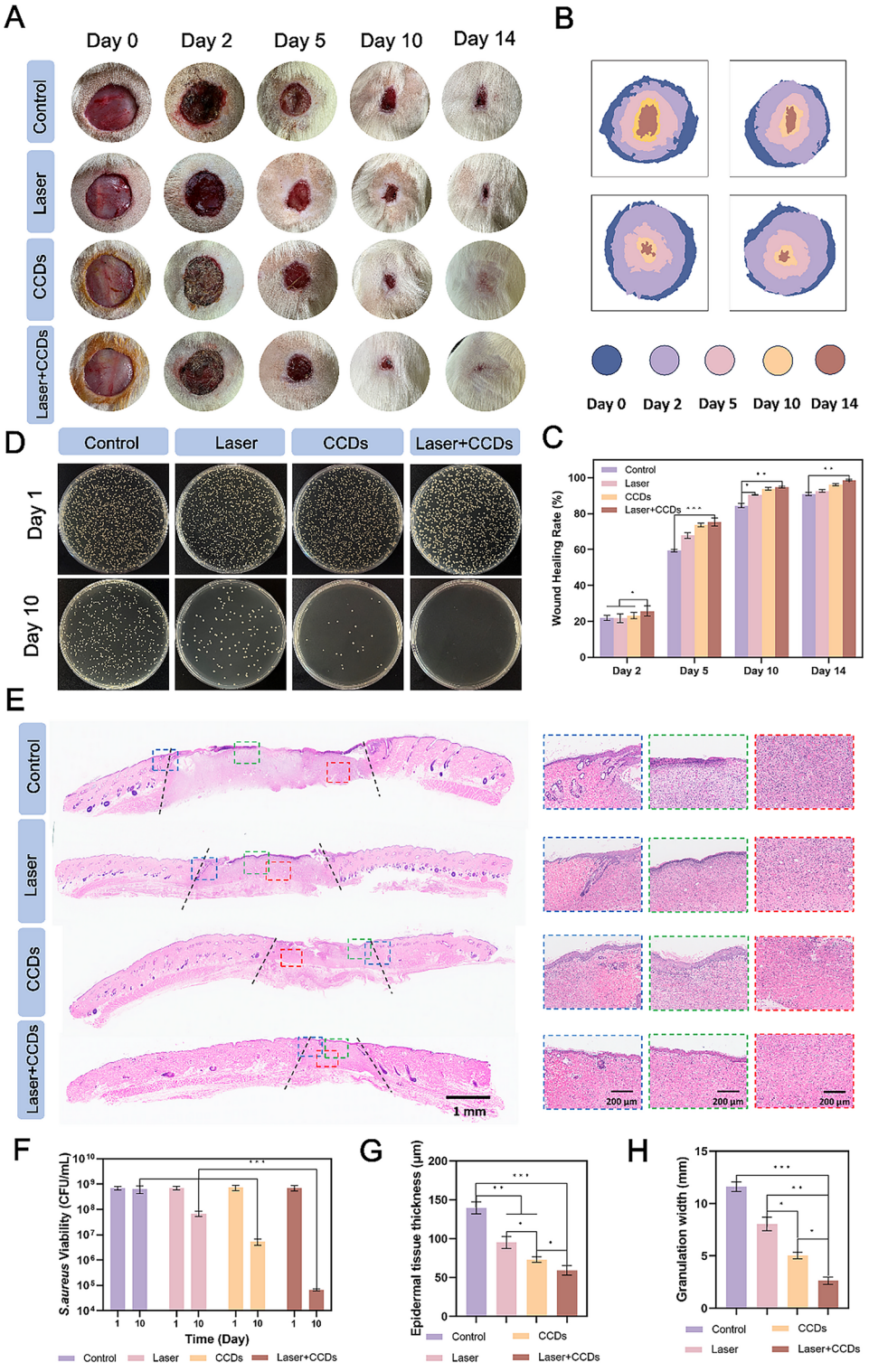

Fig. 7 Infected wounds healing *in vivo*. (**A**) Representative digital photographs of each group of wounds at day 0, 2, 5, 10, and 14; (**B**) Schematic representation of overlapping wound areas at representative time points; (**C**) Quantification of the closed wound area percentage; (**D**) Plate count images of *S. aureus* of wounds in each group at day 1 and 10; (**E**) Representative images of the H&E staining in each group, showing skin tissue, the overall structure of the neoplastic epithelium at the wound edge (in the blue dashed box), the epithelium in the center of the wound (in the red dashed box), and the subepithelial layer (in the green dashed box); (**F**) Quantitative analysis of the number of *S. aureus* colonies in each group; (**G**) Quantitative analysis of the newborn epithelial tissue thickness and (**H**) the granulation tissue width in each group. (*$p < 0.05$, **$p < 0.01$, ***$p < 0.001$)

of scar formation. In contrast, wounds in the Control and Laser groups remained open, and the newly formed tissue was significantly thinner and redder. The percentage of wounds healed in each group of rats is quantified in Fig. 7C. Significant differences were observed between groups after 2 days, with the Control group having the slowest healing rate values at all time points. 92.65%, 96.05%, and 98.7% of wounds were healed at the last time point in the Laser group, the CCDs group, and the Laser + CCDs group, respectively. To directly characterize the infection, tissues from the wound area were homogenized and incubated on agar plates. Fig. 4D and F showed the colony diagrams and quantitative results of localized bacteria in all wounds after day 1 and day 10, respectively. The results showed that a large number of colonies with surface bacterial colonization and growth were observed in all treatment groups at day 1. Whereas, on day 10, the number of colonies in the Laser + CCDs group was significantly reduced, and quantification showed that *S. aureus* was reduced by almost 4 orders of magnitude. The above results indicated that PDT with CCDs has the potential to control wound infection and assist healing.

In addition, to further explore the complex biological processes including inflammation, proliferation, and remodeling during the healing of infected wounds treated with CCDs.

in PDT, we evaluated the histological changes after 14 days. At day 14 post-treatment, hematoxylin-eosin (H&E) staining of the wound and surrounding area showed histologically relevant wound healing, such as epithelial re-formation and granulation tissue, as shown in Fig. 7E. The results of the H&E staining of the wound and surrounding area showed that the wound healing process was not as simple as that of the Control group. The granulation tissue width (distance between the black dotted lines) was significantly reduced in the CCDs group and narrowest in the Laser + CCDs group compared to the Control and Laser groups, with quantitative results showing the same trend (Fig. 7H). The blue dashed box in Fig. 7E showed the normal epithelium versus the damaged epithelium, and it can be seen that the photodynamically treated tissues appeared as smooth and flat epithelium with neoplastic hair follicles, which is closer to the state of normal skin. In contrast, the other treatment groups had disorganized cells in the basal layer, disorganized collagen, and clear demarcation from the normal epithelium. The red dashed box illustrated the reduction of inflammatory cell infiltration and the appearance of more fibroblast migration in the epithelium in the Laser + CCDs group after photodynamic treatment. The green dashed box showed that the control group had edema, discontinuity and dense inflammatory cell bands in the epithelium. The Laser + CCDs group had a thinner epithelium with no visible inflammatory cells and more mature tissue remodeling. Quantitative analysis of epithelial tissue thickness was shown in Fig. 7G. Thicker epithelial tissue thickness was observed in the Control group (138 ± 12 μm) and Laser group (94 ± 7 μm).

Collagen deposition is a key determinant of skin strength and maturity [50]. Masson staining in Fig. 8A gave a more specific picture of the amount of collagen in the newborn skin tissue and the arrangement of its fibers. The collagen fibers in the CCDs group and the Laser + CCDs treatment group were more dense, well-arranged, and the tissue was more mature. Quantitative analysis of collagen deposition in Fig. 8D showed the same results. The major collagens in the skin are collagen types I and III, which make up about 95% of the skin's collagen composition. These two types of collagens play an important role in maintaining the elasticity, integrity and pliability of the skin. Not only that, but these two most important types of collagens are also under dynamic change during the wound healing process in addition to the increase in the overall amount of collagen [51]. Therefore, Sirius red staining was utilized to differentially stain mainly type I (red/yellow) and type III (green) collagens based on the different characteristics of collagen polymerization winding and helical arrangement. The results showed (Fig. S11) that at day 7, a lower proportion of type I and type III collagen was observed in the Laser + CCDs group, with an overall green-dominated fluorescent signal, which was due to the fact that type III collagen was more predominant in the early wound healing stage. In the process of wound remodeling and tissue maturation, type III collagen was gradually replaced by mature type I. The Laser + CCDs group showed a similar proportion of type I and type III collagen as normal skin on day 14, and the overall fluorescence signal was reddish-yellow, which indicated that the wound healing after PDT tended to be normalized during reconstruction and remodeling, and there was no delayed and disordered collagen deposition.

The blood vessels in the new tissue can deliver essential nutrients, growth factors and oxygen to the wound site, and CD31 is a typical marker for vascular endothelial cells [52]. As shown in Fig. 8B, the immunofluorescence images showed that the Control and Laser groups showed few green fluorescent signals, while the CCDs and Laser + CCDs treatment groups showed more signals and more complete green fluorescent rings. Therefore, we analyzed the number and diameter of blood vessels (Fig. 8E and F) and found that can CCDs group and Laser + CCDs treatment group promoted the formation of vascular system. Zn^{2+} in the composite nanoparticles induced proliferation, migration and angiogenesis of epidermal and endothelial cells [53]. The inflammatory response period is a stage in normal wound healing, and we explored the inflammatory changes during wound healing by evaluating two typical inflammation-related

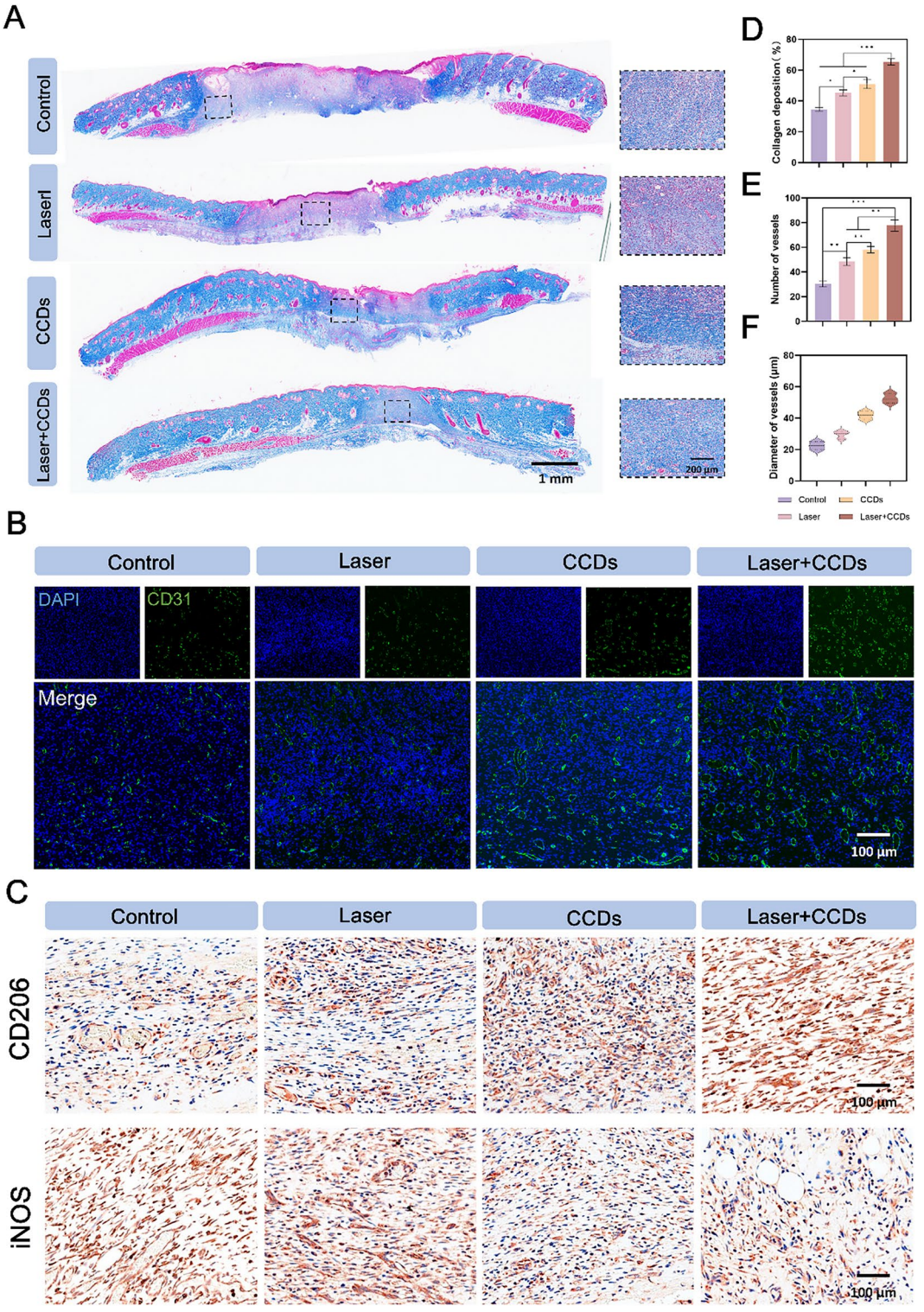

Fig. 8 (**A**) Representative images of Masson staining; (**B**) Immunofluorescence staining images of CD31 expression in each group; (**C**) Representative immunohistochemical staining images of CD206 and iNOS expression in each group; (**D**) Quantitative analysis of collagen deposition in each group; (**E**) Quantitative analysis of blood vessel number and (**F**) diameter in each group. (*$p < 0.05$, **$p < 0.01$, ***$p < 0.001$)

factors. In Fig. 8C, the anti-inflammatory factor CD206 was shown to be barely expressed in the control group, while the expression showed an increasing trend in the Laser, CCDs and Laser + CCDs treatment groups, and the pro-inflammatory factor iNOS showed a completely opposite expression in the four treatment groups. The indication suggested that PDT effectively increased the anti-inflammatory level in vivo and significantly reduced inflammation. The above results suggested that CCDs promote healing of infected wounds by accelerating the blood supply for neovascularization as well as decreasing the level of inflammation through photodynamic therapy. At the end of the animal experiments, H&E staining of major organs was performed (Fig. S14). There were no differences between all treatment groups, suggesting that CCDs were non-toxic and well biologically safe in vivo and can significantly promote infected wound healing in a safe manner.

Conclusion

Wound healing is an extremely complex process involving the integration of multiple mechanisms at different intervals on the timeline. Bacterial infections create an even longer healing cycle for wound healing. We have developed a fascinating new photosensitizer for PDT to be applied in a safe and efficient manner for the healing treatment of infected wounds. The therapeutic foundation of CCDs is laid by using curcumin, which has antibacterial and anti-inflammatory efficacy, as a raw material, and combining it with sustainably releasable Zn^{2+} to promote vascular regeneration and tissue repair as well as antimicrobial properties, we have achieved the effect of generating ROS photodynamic killing of bacteria under laser irradiation to promote the healing of infected wounds. Meanwhile, the Zn^{2+}-doped CCDs composite nanoparticles can promote the proliferation of vascular endothelial cells, alleviate tissue inflammation, and create a relatively suitable environment for wound healing. During in vivo treatment, almost complete wound healing can be achieved. What's more, the ultra-small-sized CCDs have good biocompatibility and do not cause substantial inflammation or pathological damage to normal tissues. Overall, this work will brighten the clinical application of carbon dots as antibiotic-free nanoplatforms for wound sterilization and healing.

Supplementary Information

The online version contains supplementary material available at https://doi.org/10.1186/s12951-025-03509-5.

Supplementary Material 1

Acknowledgements

Some of the schematic diagrams in the review article were created on the website https://www.figdraw.com/. We appreciate the platform's contribution.

Author contributions

Jia Liu, Lingxiang Sun and Bing Li selected the topic and guided the review, Yifan Zhao, Xi Chen and Yilin Ping wrote the manuscript, Haiyan Liu, Xuedong Deng, Wenze Han, Jing Wang, Feng Tian, Jingyu Yan and Xiuping Wu searched the references and revised the manuscript. All authors read and approved the final manuscript.

Funding

This work was supported by the Creation of hydroxyapatite-loaded chalcogenide quantum dot fluorescent probes and study of FLISA method for saliva detection, Shanxi Province Returned Overseas Students Research Project, No. 2022 – 120; The Central Government Guided Local Science and Technology Development Funds (Transfer and Transformation of Scientific and Technological Achievements) Project, No. YDZJSX2022C029; Shanxi Provincial Science and Technology Innovation Key Talent Team Project, No. 202204051002034; Graduate Student Research Innovation Program in Shanxi Province, No.2023KY416 and Shanxi Provincial Basic Research Program (Free Exploration), NO. 202203021222263.

Data availability

No datasets were generated or analysed during the current study.

Declarations

Ethics approval and consent to participate

None.

Consent for publication

All authors have given consent for publication.

Competing interests

The authors declare no competing interests.

Author details

[1]School and Hospital of Stomatology, Shanxi Medical University, Taiyuan 030001, China
[2]Shanxi Province Key Laboratory of Oral Diseases Prevention and New Materials, Taiyuan 030001, China

Received: 24 February 2025 / Accepted: 28 May 2025
Published online: 07 June 2025

References

1. John JV, Sharma NS, Tang G, Luo Z, Su Y, Weihs S, Shahriar SMS, Wang G, McCarthy A, Dyke J et al. Nanofiber aerogels with precision macrochannels and LL-37-Mimic peptides synergistically promote diabetic wound healing. Adv Funct Mater 2023;33.
2. Ghomi ER, Lakshminarayanan R, Chellappan V, Verma NK, Chinnappan A, Neisiany RE, Amuthavalli K, Poh ZS, Wong BHS, Dubey N, et al. Electrospun aligned pcl/gelatin scaffolds mimicking the skin ECM for effective antimicrobial wound dressings. Adv Fiber Mater. 2023;5:235–51.
3. Hofer U. Antibiotics predispose to nosocomial infections. Nat Rev Microbiol. 2022;20:445.
4. Chen Q, Dan H, Tang F, Wang J, Li X, Cheng J, Zhao H, Zeng X. Photodynamic therapy guidelines for the management of oral leucoplakia. Int J Oral Sci. 2019;11:14.
5. Wang S, McCoy CP, Li P, Li Y, Zhao Y, Andrews GP, Wylie MP, Ge Y. Carbon dots in photodynamic/photothermal antimicrobial therapy. Nanomaterials (Basel) 2024;14.
6. Sun L, Zhao Y, Peng H, Zhou J, Zhang Q, Yan J, Liu Y, Guo S, Wu X, Li B. Carbon Dots as a novel photosensitizer for photodynamic therapy of cancer and bacterial infectious diseases: recent advances. J Nanobiotechnol. 2024;22:210.
7. Pillar-Little TJ, Wanninayake N, Nease L, Heidary DK, Glazer EC, Kim DY. Superior photodynamic effect of carbon quantum Dots through both type I and type II pathways: detailed comparison study of top-down-synthesized and bottom-up-synthesized carbon quantum Dots. Carbon. 2018;140:616–23.
8. Chen S, Sun T, Zheng M, Xie Z. Carbon Dots based nanoscale covalent organic frameworks for photodynamic therapy. Adv Funct Mater. 2020;30:2004680.

9. Liu H, Zhong X, Pan Q, Zhang Y, Deng W, Zou G, Hou H, Ji X. A review of carbon Dots in synthesis strategy. Coord Chem Rev. 2024;498:215468.
10. Gao F, Liu J, Gong P, Yang Y, Jiang Y. Carbon Dots as potential antioxidants for the scavenging of multi-reactive oxygen and nitrogen species. Chem Eng J. 2023;462:142338.
11. Zeng M, Wang Y, Liu M, Wei Y, Wen J, Zhang Y, Chen T, He N, Fan P, Dai X. Potential efficacy of herbal Medicine-Derived carbon Dots in the treatment of diseases: from mechanism to clinic. Int J Nanomed. 2023;18:6503–25.
12. Yan H, Li P, Wen F, Xu Q, Guo Q, Su W. Green synthesis of carbon quantum Dots from plant turmeric holds promise as novel photosensitizer for in vitro photodynamic antimicrobial activity. J Mater Res Technol. 2023;22:17–34.
13. Song X, Zhang M, Dai E, Luo Y. Molecular targets of Curcumin in breast cancer (Review). Mol Med Rep. 2019;19:23–9.
14. Kotha RR, Luthria DL. Curcumin: biological, pharmaceutical, nutraceutical, and analytical aspects. Molecules 2019;24.
15. Jarosz M, Olbert M, Wyszogrodzka G, Młyniec K, Librowski T. Antioxidant and anti-inflammatory effects of zinc. Zinc-dependent NF-κB signaling. Inflammopharmacology. 2017;25:11–24.
16. Xia P, Lian S, Wu Y, Yan L, Quan G, Zhu G. Zinc is an important inter-kingdom signal between the host and microbe. Vet Res. 2021;52:39.
17. Dwivedi S, Wahab R, Khan F, Mishra YK, Musarrat J, Al-Khedhairy AA. Reactive oxygen species mediated bacterial biofilm Inhibition via zinc oxide nanoparticles and their statistical determination. PLoS ONE. 2014;9:e111289.
18. Fu J, Zhu Q, Chen Z, Zhao J, Wu S, Zhao M, Xu S, Lai D, Fu G, Zhang W. Polydopamine (PDA) coatings with endothelial vascular growth factor (VEGF) immobilization inhibiting neointimal formation post zinc (zn) wire implantation in rat aortas. Biomater Res. 2023;27:84.
19. Liu Y, He M, Yuan Y, Nie C, Wei K, Zhang T, Chen T, Chu X. Neutrophil-Membrane-Coated biomineralized Metal-Organic framework nanoparticles for atherosclerosis treatment by targeting gene Silencing. ACS Nano. 2023;17:7721–32.
20. Wu Y, Liao Q, Wu L, Luo Y, Zhang W, Guan M, Pan H, Tong L, Chu PK, Wang H. ZnL(2)-BPs integrated bone scaffold under sequential photothermal mediation: A Win-Win strategy delivering antibacterial therapy and fostering osteogenesis thereafter. ACS Nano. 2021;15:17854–69.
21. Marković ZM, Jovanović SP, Mašković PZ, Danko M, Mičušík M, Pavlović VB, Milivojević DD, Kleinová A, Špitalský Z. Todorović Marković BM: Photo-induced antibacterial activity of four graphene based nanomaterials on a wide range of bacteria. RSC Adv. 2018;8:31337–47.
22. Travlou NA, Giannakoudakis DA, Algarra M, Labella AM, Rodríguez-Castellón E, Bandosz TJ. S- and N-doped carbon quantum dots: surface chemistry dependent antibacterial activity. Carbon. 2018;135:104–11.
23. Lu S, Chen Z, Tu H, Liu H, Liu Y, Chen S, Cai D, Liu C, Zhang X, Zou G, et al. Multifunctional carbon quantum Dots decorated self-healing hydrogel for highly effective treatment of Superbug infected wounds. Chem Eng J. 2024;480:148218.
24. Hu R, Zhai X, Ding Y, Shi G, Zhang M. Hybrid supraparticles of carbon dots/porphyrin for multifunctional tongue-mimic sensors. Chin Chem Lett. 2022;33:2715–20.
25. Qu X, Gao C, Fu L, Chu Y, Wang JH, Qiu H, Chen J. Positively charged carbon Dots with antibacterial and antioxidant dual activities for promoting infected wound healing. ACS Appl Mater Interfaces. 2023;15:18608–19.
26. Li Y, Zheng W, Zhang H, Wang H, Cai H, Zhang Y, Yang Z. Electron transfer mechanism of graphene/cu heterostructure for improving the stability of triboelectric nanogenerators. Nano Energy. 2020;70:104540.
27. Huo F, Liu Y, Zhu M, Gao E, Zhao B, Yang X. Ultrabright full color carbon Dots by Fine-Tuning crystal morphology controllable synthesis for multicolor bioimaging and sensing. ACS Appl Mater Interfaces. 2019;11:27259–68.
28. Desai MA, Sharma V, Prasad M, Gund G, Jadkar S, Sartale SD. Photoelectrochemical performance of MWCNT–Ag–ZnO ternary hybrid: a study of ag loading and MWCNT garnishing. J Mater Sci. 2021;56:8627–42.
29. Han B, Wang W, Wu H, Fang F, Wang N, Zhang X, Xu S. Polyethyleneimine modified fluorescent carbon Dots and their application in cell labeling. Colloids Surf B Biointerfaces. 2012;100:209–14.
30. Costa SS, Ribeiro R, Serrano M, Oliveira K, Ferreira C, Leal M, Pomba C, Couto I. Staphylococcus aureus causing skin and soft tissue infections in companion animals: antimicrobial resistance profiles and clonal lineages. Antibiot (Basel) 2022;11.
31. Saheb Kashaf S, Harkins CP, Deming C, Joglekar P, Conlan S, Holmes CJ, Almeida A, Finn RD, Segre JA, Kong HH. Staphylococcal diversity in atopic dermatitis from an individual to a global scale. Cell Host Microbe. 2023;31:578–e592576.
32. Lam PL, Lee KKH, Wong RSM, Cheng GYM, Bian ZX, Chui CH, Gambari R. Recent advances on topical antimicrobials for skin and soft tissue infections and their safety concerns. Crit Rev Microbiol. 2018;44:40–78.
33. Alharbi NS, Khaled JM, Kadaikunnan S, Alobaidi AS, Sharafaddin AH, Alyahya SA, Almanaa TN, Alsughayier MA, Shehu MR. Prevalence of Escherichia coli strains resistance to antibiotics in wound infections and Raw milk. Saudi J Biol Sci. 2019;26:1557–62.
34. Yu D, Zha Y, Zhong Z, Ruan Y, Li Z, Sun L, Hou S. Improved detection of reactive oxygen species by DCFH-DA: new insight into self-amplification of fluorescence signal by light irradiation. Sens Actuators B. 2021;339:129878.
35. Yang Q-Q, Farha AK, Kim G, Gul K, Gan R-Y, Corke H. Antimicrobial and anticancer applications and related mechanisms of curcumin-mediated photodynamic treatments. Trends Food Sci Technol. 2020;97:341–54.
36. Wei Y, Wang J, Wu S, Zhou R, Zhang K, Zhang Z, Liu J, Qin S, Shi J. Nanomaterial-Based zinc ion interference therapy to combat bacterial infections. Front Immunol. 2022;13:899992.
37. Pandey M, Singh AK, Pandey PC. Synthesis and in vitro antibacterial behavior of curcumin-conjugated gold nanoparticles. J Mater Chem B. 2023;11:3014–26.
38. Hamblin MR, O'Donnell DA, Murthy N, Rajagopalan K, Michaud N, Sherwood ME, Hasan T. Polycationic photosensitizer conjugates: effects of chain length and gram classification on the photodynamic inactivation of bacteria. J Antimicrob Chemother. 2002;49:941–51.
39. Sobotta L, Skupin-Mrugalska P, Piskorz J, Mielcarek J. Porphyrinoid photosensitizers mediated photodynamic inactivation against bacteria. Eur J Med Chem. 2019;175:72–106.
40. Abraham WL, Demirci S, Wypyski MS, Ayyala RS, Bhethanabotla VR, Lawson LB, Sahiner N. Biofilm Inhibition and bacterial eradication by C-dots derived from polyethyleneimine-citric acid. Colloids Surf B. 2022;217:112704.
41. Lapinska B, Konieczka M, Zarzycka B, Sokolowski K, Grzegorczyk J, Lukomska-Szymanska M. Flow cytometry analysis of antibacterial effects of universal dentin bonding agents on streptococcus mutans. Molecules 2019;24.
42. Han X, Chen S, Cai Z, Zhu Y, Yi W, Guan M, Liao B, Zhang Y, Shen J, Cui W, Bai D. A diagnostic and therapeutic hydrogel to promote vascularization via blood sugar reduction for wound healing. Adv Funct Mater. 2023;33:2213008.
43. Nowak-Sliwinska P, van Beijnum JR, Griffioen CJ, Huinen ZR, Sopesens NG, Schulz R, Jenkins SV, Dings RPM, Groenendijk FH, Huijbers EJM, et al. Proinflammatory activity of VEGF-targeted treatment through reversal of tumor endothelial cell anergy. Angiogenesis. 2023;26:279–93.
44. Stratman AN, Farrelly OM, Mikelis CM, Miller MF, Wang Z, Pham VN, Davis AE, Burns MC, Pezoa SA, Castranova D, et al. Anti-angiogenic effects of VEGF stimulation on endothelium deficient in phosphoinositide recycling. Nat Commun. 2020;11:1204.
45. Chen Z, Duan J, Diao Y, Chen Y, Liang X, Li H, Miao Y, Gao Q, Gui L, Wang X, et al. ROS-responsive capsules engineered from EGCG-Zinc networks improve therapeutic angiogenesis in mouse limb ischemia. Bioact Mater. 2021;6:1–11.
46. Zhang B, Wan H, Liu X, Yu T, Yang Y, Dai Y, Han Y, Xu K, Yang L, Wang Y, Zhang X. Engineering Immunomodulatory stents using zinc Ion-Lysozyme nanoparticle platform for vascular remodeling. ACS Nano. 2023;17:23498–511.
47. Krizanova O, Penesova A, Sokol J, Hokynkova A, Samadian A, Babula P. Signaling pathways in cutaneous wound healing. Front Physiol. 2022;13:1030851.
48. Sun Y, Liu WZ, Liu T, Feng X, Yang N, Zhou HF. Signaling pathway of MAPK/ERK in cell proliferation, differentiation, migration, senescence and apoptosis. J Recept Signal Transduct Res. 2015;35:600–4.
49. Wei X, Wang J, Deng YY, Shao BH, Zhang ZF, Wang HH, Wang CM. Tubiechong patching promotes tibia fracture healing in rats by regulating angiogenesis through the VEGF/ERK1/2 signaling pathway. J Ethnopharmacol. 2023;301:115851.
50. Xu Q, Dai W, Li P, Li Q, Gao Z, Wu X, Liu W, Wang W. Piezoelectric film promotes skin wound healing with enhanced collagen deposition and vessels regeneration via upregulation of PI3K/AKT. Nano Res. 2024;17:7461–78.
51. Hao R, Ye X, Chen X, Du J, Tian F, Zhang L, Ma G, Rao F, Xue J. Integrating bioactive graded hydrogel with radially aligned nanofibers to dynamically manipulate wound healing process. ACS Appl Mater Interfaces. 2024;16:37770–82.
52. Cheung KCP, Fanti S, Mauro C, Wang G, Nair AS, Fu H, Angeletti S, Spoto S, Fogolari M, Romano F, et al. Preservation of microvascular barrier function requires CD31 receptor-induced metabolic reprogramming. Nat Commun. 2020;11:3595.
53. Yao J, Huang C, Yao J, Hui J, Shen S, Zheng X, Shen L, Fan D. A moldable hydrogel based on sericin and Zn2+/F- dual-doped hydroxyapatite promotes

skull defect repair through the synergistic effects of immunoregulation, enhanced angiogenesis and osteogenesis. Chem Eng J. 2024;491:151789.

Publisher's note